Hindawi
Mathematical Problems in Engineering
Volume 2019, Article ID 8913956, 14 pages
https://doi.org/10.1155/2019/8913956

*Research Article*

# The Research on Bus Voltage Stabilization Control of Off-Grid Photovoltaic DC Microgrid under Impact Load

**Yu Zhang**,[1,2,3] **Ziguang Lu**,[1] **Quan Lu**,[1,3] **and Shuhao Wei**[2]

[1] *The College of Electrical Engineering, Guangxi University, Nanning 530004, China*
[2] *The College of Mechanical and Control Engineering, Guilin University of Technology, Guilin 541004, China*
[3] *Guangxi Key Laboratory of Building New Energy and Energy Saving, Guilin 541004, China*

Correspondence should be addressed to Quan Lu; luquan@gxu.edu.cn

Received 4 April 2019; Revised 31 May 2019; Accepted 4 June 2019; Published 24 June 2019

Academic Editor: Sajad Azizi



The solar power generation includes certain randomness and volatility, coupled with dynamic load involved in power fluctuations, which renders microgrid having certain unplanned instantaneous power during the process of real-time operation, so as to affect the stability of DC bus voltage. This paper, through constructing a model of off-grid photovoltaic DC microgrid under impact load characteristics, aiming at the fluctuate problems of the DC bus voltage caused by impact load, puts forward a fast response of hybrid energy-storing system composed of supercapacitors and batteries and superiors peak regulation capability to shave the peak and fill the valley of the microgrid. The researches on the strategy of double closed-loop voltage stabilization of blended energy storage system are made and the shortcomings of the double closed-loop voltage control of voltage and electricity are analyzed. And based on this, the tactics of new and double closed-loop voltage control of inner ring of power and the energy outer ring of DC bus capacitance are put forward and examined by simulation and experiment. The experiments prove that this method can more effectively suppress the influence of the fluctuations of impact load power on the DC bus voltage and further improves the system's stability.

## 1. Introduction

Affected by the randomness and volatility of solar power generation, the photovoltaic power generation is difficult to accurately predict, and added with the power fluctuations containing dynamic load, the microgrid produces some instantaneous fluctuation power beyond project during the practical running, which results in increasing system' losses, overloading transformer, overheating electrical machinery, protecting the failure of malfunctioning and sensitive equipment, and even limiting the distributed output power of power supply [1, 2]. Particularly, when the microgrid is functioning independently, it is short of the support of the large power grid. Hence, it is significant how to speedily balance the unplanned instant power fluctuation of the microgrid and keep the stability of the DC bus voltage of the microgrid to ensure the electric quality.

Currently, the fluctuations of DC bus voltage triggered by the mismatch between output power and load power of photovoltaic DC Microgrid are mainly compensated through the blended energy storage system combined by storage batteries and supercapacitors, which can make full use of the high energy density of storage battery and the high power density of supercapacitor to meet the technical requirements of different levels [3–5]. Scholars have done a lot of researches that set the studying hot spot as focusing on the control tactics to the energy storage unit DC/DC converter [6–8].

With regard to the control strategy problems of energy storage unit DC/DC converter, most of them adopt the voltage-current double closed-loop control [9, 10] or its improved strategy [11–17]. It takes the DC bus voltage as the control outer ring and the inductor current of the energy storage unit as the control inner ring in the voltage-current double closed-loop control, where it is difficult to restrain the effects of high-power disturbance on the DC bus voltage in a short time.

In order to increase the antijamming performance of DC/DC converter, many scholars have introduced the

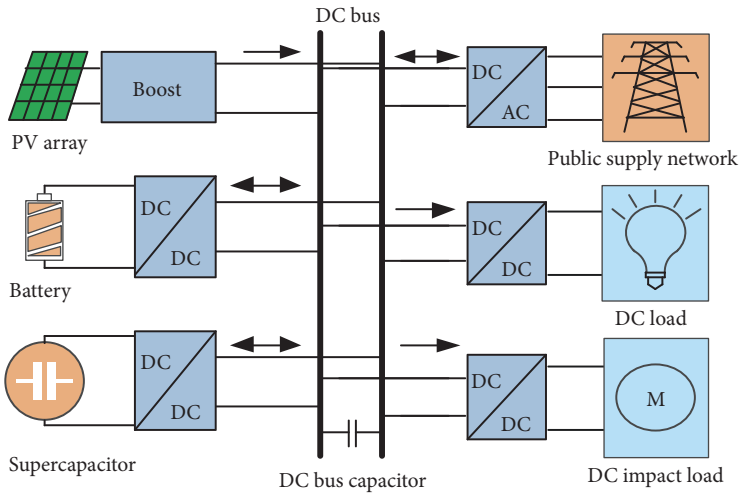


Figure 1: Topology structure of photovoltaic DC microgrid.

method of feedforward control into the traditional double closed-loop control [18–21], of which the reference value of current inner ring is able to quickly track the external disturbance to upgrade the dynamic response performance of the system. The feedforward can be divided into current feedforward and power feedforward [22] according to the different feedforward variables. Kouro S, Dong Dong, Guo Li et al. [23–25] adopted current feedforward control method to reduce DC voltage fluctuation caused by external disturbance, under which the impacts that load current exerts on the DC bus voltage are eliminated by reasonably configuring feedforward coefficients. However, because of the lag of the voltage loop and the delay of the current loop, the response from output current will lag behind the load disturbance. Mademlis G, Sato A et al. [22, 26] utilized power feedforward control strategy; in other words, feedforward link of disturbance power is brought in the current inner ring, which accelerates the response speed of the system to the power disturbance and lowers the DC side voltage fluctuation triggered by load disturbance. This approach makes the current loop rapidly track the external power disturbance, to some extent, restraining the voltage fluctuation of DC bus. But like the current feedforward, the power feedforward also has to pass the current control ring, and under that, the output current still lags behind. The feedforward control needs to collect the real-time information of multiple microsources and loads synchronously, which will increase cost and reduce reliability of the system, and it is not conducive to the expansion of microgrid system. Viewing on this situation, Ibrahim O, Wang Chengshan et al. [27, 28] brought observation methods such as state observer and nonlinear disturbance observer into the control loop, so as to measure the required parameters. Besides, based on this, the feedforward control is adopted to enhance the systematic stability margin and dynamic response characteristics simultaneously. But when using the state variables of the observer Observation system, the noises are inevitably added and affect the electric quality of the microgrid.

The above upgraded strategies of the double closed-loop control improve the system's ability to suppress bus voltage fluctuation, whereas these control means are only optimized under the traditional voltage-current double closed-loop control, which has limited the improved inhibition effects on the bus voltage fluctuation. In the past, the steady voltage control of the DC bus was a study that was mainly carried on under the situation of small fluctuations in conventional load power. And the steady voltage control of the DC bus rarely referred to the impact of sudden access of impulsive load on DC bus voltage. On the basis of the above situation, this paper vitally studies the voltage stable of DC/DC bus under the impact load and optimizes the control strategies of the DC converter of energy-storing unit, which makes innovations and contributions as the follows:

(1) The model of photovoltaic DC microgrid is established under impact load characteristics, and its uncertainty elements are analyzed.

(2) Following the study of the control strategy of the DC bus based on the impact load, a new double closed-loop control strategy, with the output power of energy-storing system converter as the control inner ring and the capacitance energy of the DC bus as the control outer ring, is put forward. This strategy directly commands the capacitance energy of bus, so as to adjust the stable voltage of DC bus and improve the dynamic response performance.

(3) The related simulations and experiments are conducted to prove the effectiveness of the control strategy of the power inner ring and energy outer ring.

## 2. Model Establishment

The topological structure of photovoltaic DC microgrid adopted in this paper is mainly composed of photovoltaic cell, battery, supercapacitor, loads, and converters, as shown in Figure 1. The photovoltaic cell is connected with the DC bus through the Boost booster circuit. Moreover, the supercapacitor and the battery make up the hybrid energy

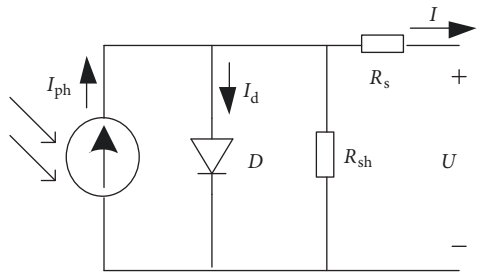


Figure 2: Equivalent circuit of photovoltaic cell.

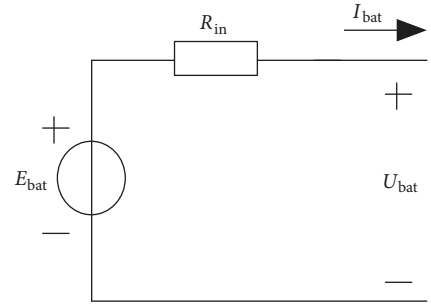


Figure 3: The equivalent circuit of battery.

storage system and both of them parallel to the DC bus through the bidirectional Buck/Boost Converter (BDC). This paper employs the DC impact load.

*2.1. Photovoltaic Model.* Photovoltaic cell is made up of semiconductor diodes, and its operating principle is the photovoltaic effect. The P-N knot of semiconductor switches light energy into electrical energy under the sunlight exposure, of which the output power is mainly affected by solar irradiance, the surface temperature of photovoltaic panel, and other factors. The equivalent model is shown in Figure 2 [29].

According to the equivalent circuit of photovoltaic cells, the output characteristic equation $I - U$ of photovoltaic cells is shown as

$$I = I_{ph} - I_o \left[ \exp \frac{q\left(U + IR_s\right)}{nKT} - 1 \right] - \frac{U + IR_s}{R_{sh}}. \quad (1)$$

Among them,

$$I_{ph} = \frac{G}{G_0} I_{g0}, \quad (2)$$

where $I$ indicates the photovoltaic cell' output electrical current (A), $I_{ph}$ is the optical current (A), $I_o$ refers to the reverse saturation current (A) without illumination, $I_{g0}$ indicates the motivate current (A) under the standard illumination intensity, $U$ is the output voltage (V) of the photovoltaic cell, $q$ represents the constant of electron charge, of which the value is $q = 1.6 \times 10^{-19}$C, $n$ is the factor of diode curve, $K$ is on behalf of the Boltzmann constant, $K = 1.38 \times 10^{-23}$, $T$ refers to the absolute temperature (K) on surface of the solar cell, $G_0$ means the standard illumination intensity (W/m$^2$), $G$ is the illumination intensity (W/m$^2$), $R_s$ indicates the series resistance (Ω), and $R_{sh}$ serves as the parallel resistance (Ω).

*2.2. Battery Model.* The battery features in large energy density, long time storage energy, and slow response, which primarily bears the load and peak shaving and valley filling in the microgrid. The mathematical model of the battery in this paper utilizes the internal resistance equivalent circuit. The battery is equivalent to the series connection between the ideal voltage source and resistance, and the circuit is demonstrated in Figure 3.

In Figure 3, $E_{bat}$ indicates an empty load voltage (V); $I_{bat}$ means that the battery charges and discharges current (A); $R_{in}$ acts as an internal equivalent resistance (Ω); $U_{bat}$ is terminal voltage (V) of battery. The formula for the voltage source $E_{bat}$ is

$$E_{bat} = E_0 - k \cdot \frac{Q}{Q - \int_0^t idt} + A \exp\left(-B \cdot \int_0^t idt\right). \quad (3)$$

In the formula, $E_0$ represents constant voltage (V) of the battery; $k$ is polarization voltage (V); $Q$ represents the capacity of battery; $\int_0^t idt$ means the actual charge amount; $A$ represents the amplitude value of the exponential region; $B$ means the reciprocal inverse of the time constant within exponential region. According to the curve of the battery discharging, the voltage $E_{nom}$ and capacity $Q_{nom}$ of the end point within standard discharging area can be obtained.

Then, the expressing equation of the internal equivalent resistance and output voltage of the battery are

$$R_{in} = E_{nom} \cdot \frac{1 - \eta}{0.2Q_{nom}} \quad (4)$$

$$U_{bat} = E_{bat} - R_{in} \cdot I_{bat}, \quad (5)$$

where $\eta$ is the efficient coefficient of battery, and its value is $\eta = 0.995$.

*2.3. Supercapacitor Model.* The supercapacitor has relatively large power density and chiefly undertakes the high-frequency power fluctuations in the DC microgrid. Especially under the interference of impact load, the supercapacitor can play the role of peak shaving and valley filling, maintain the stability of DC bus voltage, reduce the times of battery charging and discharging, and lower the cost of the DC microgrid. This paper applies a circuit model of series RC and its equivalent circuit is shown in Figure 4 [30].

According to Figure 4, the characteristic equation $I - U$ of supercapacitor is established as

$$U_{sc} = I_{sc}R_{sc} + \frac{1}{C} \int I_{sc} dt, \quad (6)$$

where $U_{sc}$ indicates the output voltage (V) of the supercapacitor; $I_{sc}$ is the output current (A) of the supercapacitor; $R_{sc}$ and $C$ represent the equivalent resistance and equivalent

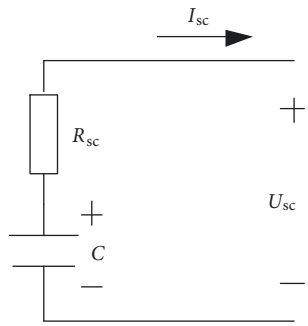


Figure 4: The equivalent circuit of supercapacitor.

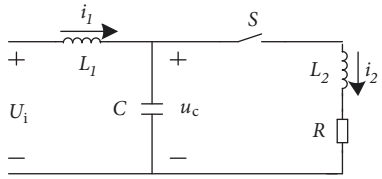


Figure 5: Impact load model.

capacitor, respectively. The energy expressions of supercapacitor and charging and discharging processes are shown in the following formulas, respectively:

$$E_{sc}(kt) = E_{sc}[(k-1)t] + P_{sc}(kt) \times t \times n_{scc} \tag{7}$$

$$E_{sc}(kt) = E_{sc}[(k-1)t] + P_{sc}(kt) \times t \times n_{scd}, \tag{8}$$

where $E_{sc}(kt)$ and $E_{sc}[(k-1)t]$ refer to the storage energy of the supercapacitor at the moment of $kt$ and $(k-1)t$, respectively; $P_{sc}$ is the charging and discharging power (W) of the supercapacitor; $n_{scc}$ and $n_{scd}$ indicate the efficiency coefficient of charging and discharging of the supercapacitor, respectively.

*2.4. Mathematical Model of Impact Load.* In the photovoltaic DC microgrid system, the starting power of impact load may reach three times bigger than the rated power at the moment of access instantaneous. That the photovoltaic output power does not mismatch the rapid changes of load power will lead to huge fluctuations in the DC bus voltage and further cause the oscillation of power transformation system, even crashing, which is not conducive to the stable operation of the microgrid. In this paper, DC electrical machinery is selected as DC impact load, and it attaches importance to the influences of connecting DC electrical machinery and shutting moment on the bus voltage of photovoltaic DC microgrid. According to Figure 5, the DC motor is equivalent to *RL* circuit model, and *S* equals the DC switch, $L_1$, and $C$ consist of filter circuit through DC/DC converter connecting the DC bus.

Where $U_i$ represents input voltage of impact load; $i_1$ is load current (A); $i_2$ indicates the electrical machinery current (A); $u_c$ means the voltage (V) of the motor end, when the switch S is switched on, the load is connected, according to KCL and KVL, it gets

$$\begin{aligned} U_i &= L_1 \frac{di_1}{dt} + u_c \\ i_1 &= C\frac{du_c}{dt} + i_2 \\ u_c &= L_2 \frac{di_2}{dt} + i_2 R. \end{aligned} \tag{9}$$

Setting $x_1 = i_1$, $x_2 = u_c$, $x_3 = i_2$, according to formula (9), the state space equation is

$$\dot{x} = A_1 x + B_1 U_i, \tag{10}$$

where $x$ is state vector; $A_1$ is system matrix; $B_1$ is control matrix. And $x = [x_1\ x_2\ x_3]^T$.

$$\begin{aligned} A_1 &= \begin{bmatrix} 0 & \frac{-1}{L_1} & 0 \\ \frac{1}{C} & 0 & \frac{-1}{C} \\ 0 & \frac{1}{L_2} & \frac{-R}{L_2} \end{bmatrix}, \\ B_1 &= \begin{bmatrix} \frac{1}{L_1} \\ 0 \\ 0 \end{bmatrix}. \end{aligned} \tag{11}$$

When the switch S is turned off, the load is disconnected, and according to KCL and KVL, it can get

$$\begin{aligned} U_i &= L_1 \frac{di_1}{dt} + u_c \\ i_1 &= C\frac{du_c}{dt}. \end{aligned} \tag{12}$$

While the S is switched off, the state equation of the system is

$$\dot{x} = A_2 x + B_2 U_i. \tag{13}$$

Of them,

$$\begin{aligned} A_2 &= \begin{bmatrix} 0 & -\frac{1}{L_1} & 0 \\ \frac{1}{C} & 0 & 0 \\ 0 & 0 & 0 \end{bmatrix}, \\ B_2 &= \begin{bmatrix} \frac{1}{L_1} \\ 0 \\ 0 \end{bmatrix} \end{aligned} \tag{14}$$

The working cycle $T = T_{on} + T_{off}$ of the impact load is defined, in which $T_{on}$ is the conducting time of the switch and $T_{off}$ is the disconnecting time of switch. Hence, the

conducting ratio of the switch is defined as $d = T_{on}/(T_{on} + T_{off})$. Averagely weighting formula (10) and formula (13) by using the conducting ratio, a uniform state equation can be worked out:

$$\dot{x} = Ax + BU_i. \tag{15}$$

Among them,

$$A = dA_1 + (1-d)A_2 = \begin{bmatrix} 0 & -\frac{1}{L_1} & 0 \\ \frac{1}{C} & 0 & -\frac{d}{C} \\ 0 & \frac{d}{L_2} & \frac{-dR}{L_2} \end{bmatrix}. \tag{16}$$

$$B = dB_1 + (1-d)B_2 = \begin{bmatrix} \frac{1}{L_1} \\ 0 \\ 0 \end{bmatrix}.$$

*2.5. The Analysis of Uncertainty.* When the DC microgrid functions independently, the fluctuation of the photovoltaic output and the dynamic change of the load will lead to the power imbalance of the system and the voltage fluctuation of the DC bus and will affect the steady operation of the whole system. More seriously, they even give rise to the protection device action of the system and eventually completely collapse the system. The uncertainties in this paper are taken into consideration from the photovoltaic output and load power.

The power generation of photovoltaic cells is directly related to the irradiation intensity. In terms of the uncertainty analysis of the output power of photovoltaic cells, the Beta distribution function is usually adopted to describe irradiance:

$$f(G) = \frac{\Gamma(\alpha+\beta)}{\Gamma(\alpha)\Gamma(\beta)}\left(\frac{G}{G_{max}}\right)^{\alpha-1}\left(1-\frac{G}{G_{max}}\right)^{\beta-1}, \tag{17}$$

where

$$\alpha = \frac{\mu^2}{\sigma^2}(1-\mu) - \mu$$
$$\beta = \frac{1-\mu}{\mu}\alpha. \tag{18}$$

In the equation, $f(G)$ represents probability function; $G$ is real irradiance; $G_{max}$ is used as maximum irradiance; $\Gamma(\bullet)$ is Gamma function; $\alpha, \beta$ refer to figurate parameter; $\mu$ is a random variable mean; $\sigma^2$ is variance of the random variable.

If then irradiance meets

$$G_{min} < G < G_S, \tag{19}$$

where $G_{min}$ indicates the lowest irradiance and $G_S$ is rated irradiance, with taking the discrete step length as $(G_S - G_{min})/N_G$ and dividing it into $N_G$ states, then the occurred probability of each state is as follows:

$$G(i) = \left[\frac{(i-1/2)}{N_G}\right](G_S - G_{min}) + G_{min}$$
$$F_G(i) = \int_{[(i-1)/N_G](G_S-G_{min})+G_{min}}^{(i/N_G)(G_S-G_{min})+G_{min}} f(G)\,dG, \tag{20}$$

where $N_G$ is the number of states within the irradiance interval; $f(G)$ represents the probability density function of irradiance; $F_G(i)$ means the probability of the occurrence of the $i$, $i = 1, 2, \ldots, N_G$.

If the irradiance is lower than $G_{min}$, it does not meet formula (19). The photovoltaic power generation is the $N_G + 1$ state, and at that moment the probability of occurrence of the irradiance and state is as follows:

$$G(N_G+1) = 0$$
$$F_G(N_G+1) = \int_0^{G_{min}} f(G)\,dG. \tag{21}$$

However, if the irradiance is higher than $G_S$, then the photovoltaic power generation is in the $N_G + 2$, where the probability of occurrence of the state and irradiance is as follows:

$$G(N_G+2) = G_S$$
$$F_G(N_G+2) = \int_1^{+\infty} f(G)\,dG. \tag{22}$$

From the above, the photovoltaic output power and its related state probability can be calculated at each moment. The uncertainties of the load power approximately comply with the normal distribution function:

$$f(P) = \frac{1}{\sqrt{2\pi}\sigma}\exp\left[-\frac{(P-\mu)^2}{2\sigma^2}\right]. \tag{23}$$

About 99.73% value of numerical distribution is distributed within a range of 3 standard deviations from the average distance. In addition, it is assumed that the load power at each moment of the system is distributed within 3 standard deviations from the average load at that time:

$$P_L(t) \in [\mu_L(t) - 3\sigma_L(t), \mu_L(t) + 3\sigma_L(t)]. \tag{24}$$

In this equation, $P_L(t)$, $\mu_L(t)$, and $\sigma_L(t)$ represent $t$ moment load power, load mean, and load standard deviation.

By dividing the mean value of load at each moment into $N_L$ states, the probabilities of load in every state and its occurrence are as follows:

$$P_L(i) = \mu_L - 3\sigma_L + \frac{6\sigma_L(i-1/2)}{N_L}$$
$$F_L(i) = \int_{\mu_L-3\sigma_L+6\sigma_L(i-1)/N_L}^{\mu_L-3\sigma_L+6\sigma_L i/N_L} f(P_L)\,dP_L, \tag{25}$$

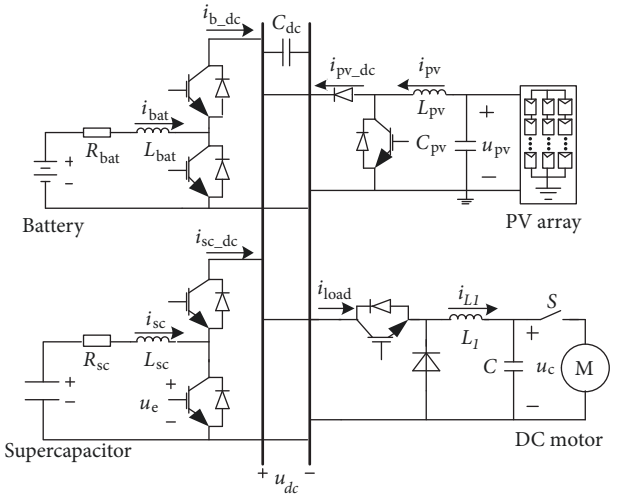


Figure 6: The main circuit structure.

where $N_L$ refers to the number of states in the load power interval; $f(P_L)$ represents the probability distribution function of load power; $F_L(i)$ is the probability that occurred by the $i$ state, $i = 1, 2, \ldots, N_L$.

In a word, the load power and its corresponding state probability can be calculated at each time.

If the stability of the DC bus voltage is to be maintained without considering the energy storage system, the photovoltaic output power is the same as the load consumption power, that is,

$$P_G(t) = P_L(t). \tag{26}$$

Among them, $P_G(t)$ is the output power of photovoltaic at the $t$ moment; $P_L(t)$ is the power consumption of load at the $t$ moment. According to the uncertainty analysis above, the system is difficult to real-timely guarantee whether (26) is valid or not. Therefore, the energy storage device is introduced to compensate the unbalanced power of the system, and formula (26) is listed as

$$P_G(t) \pm P_S(t) = P_L(t), \tag{27}$$

where $P_S(t)$ indicates the power of the energy storage system. When the symbol before $P_S(t)$ is "+", the power gets released; when the symbol before $P_S(t)$ is "-", the power is absorbed.

Comparing (26) with (27), it can be found that introducing energy storage system can better guarantee the power balance in the microgrid, thus maintaining the stability of the DC bus voltage.

## 3. The Stabilization Control of DC Bus Voltage

The main circuit structure of photovoltaic DC microgrid system in the isolated island state is shown in Figure 6. $U_{bat}$ indicates the end voltage (V) of the battery; $U_{sc}$ represents the end voltage (V) of supercapacitor; $u_e$ is the lower bridge arm collector and emitting extreme voltage (V) of the converter; $L_{bat}$ and $L_{sc}$ appear as the energy storage inductance (H) of the batteries and the supercapacitors converter, respectively; $R_{bat}$ and $R_{sc}$ show the parasitic resistance (Ω) of two inducers.

The dynamic equations on the DC bus can be gained by analyzing the circuit:

$$C_{dc}\frac{du_{dc}}{dt} = \left(i_{b\_dc} + i_{sc\_dc} + i_{pv\_dc}\right) - i_{load}, \tag{28}$$

where $C_{dc}$ refers to the DC bus capacitance; $i_{b\_dc}$, $i_{sc\_dc}$, $i_{pv\_dc}$, and $i_{load}$ accordingly represent the charging and discharging current of the DC side of battery, the charging and discharging current of the super capacitance, and the output current and load current of the photovoltaic cell; $u_{dc}$ is DC bus voltage. According to formula (28), the DC bus voltage is influenced by both the output current and load current of the photovoltaic cell. The voltage stability of the DC bus can be maintained by controlling charging and discharging current of the batteries and the supercapacitors.

When the impact load occurs in the system, the load current will make relatively large fluctuations at the moment of load starting or shutting. Therefore, the control of the energy storage system plays a key role in maintaining the voltage stability of the DC bus. And only through effectively controlling the energy storage system can it compensate or absorb the DC bus power in time to ensure the stable operation of the system.

*3.1. The Control Strategy of Classic Double Closed-Loop.* The classical double closed-loop control takes the inductance current of the batteries or the supercapacitors as the control inner ring and takes the DC bus voltage as the control outer ring, taking the supercapacitors as an example, shown in Figure 7 [8]. In the figure, $U_{dc}^*$ indicates the setting value (V) of the DC bus voltage; $P_d$ is the perturbation power (W); $G_{u1}(s)$ and $G_i(s)$ is on behalf of the transfer function of the outer ring of voltage and inner ring PI controller of the current, respectively, and $K$ is proportional gain.

According to Figure 7, the closed-loop transfer function of the inner ring controller of the current is

$$\phi_i(s) = \frac{G_i(s)}{G_i(s) + sL_{sc} + R_{sc}}, \tag{29}$$

of which,

$$\begin{aligned} G_i(s) &= K_i + \frac{T_i}{s} \\ G_{u1}(s) &= K_{u1} + \frac{T_{u1}}{s}, \end{aligned} \tag{30}$$

where $K_i$ and $T_i$ are proportional coefficient and integration coefficient of the inner ring PI controller of the current; $K_{u1}$ and $T_{u1}$ represent the ratio coefficient and integration coefficient of the PI controller of voltage outer ring. Formula (30) is put into formula (29) as

$$\phi_i(s) = \frac{K_i s + T_i}{L_{sc}s^2 + \left(R_{sc} + K_i\right)s + T_i}. \tag{31}$$

When analyzing the voltage outer ring, the current inner ring is utilized as the proportional link to simplify the analysis

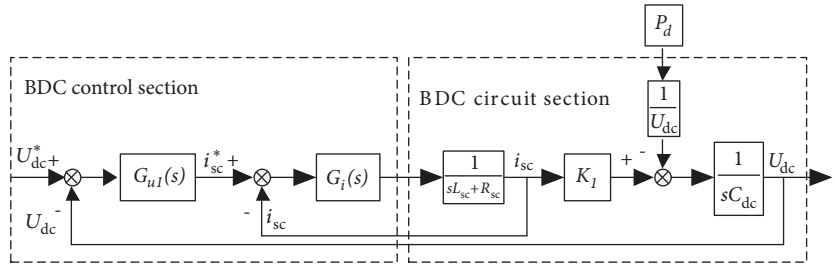


Figure 7: Control frame diagram of classic double closed-loop.

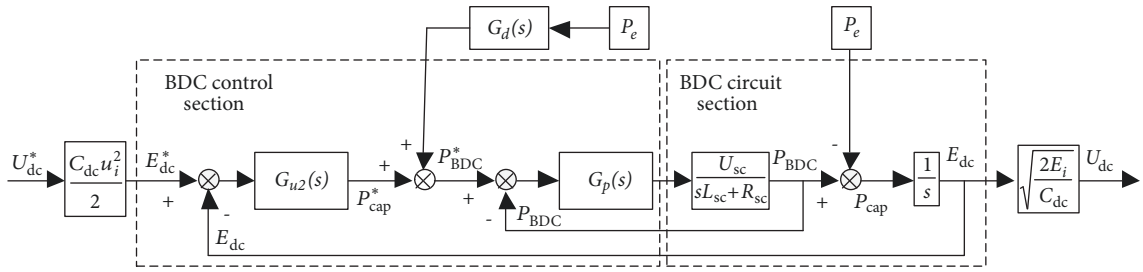


Figure 8: Power inner-loop control strategy.

process, and it is set as $K_2$, and then the transfer function of the voltage outer loop is

$$U_{dc}(s) = \frac{K_{u1}K_1K_2s + T_{u1}K_1K_2}{C_{dc}s^2 + K_{u1}K_1K_2s + T_{u1}K_1K_2}U^*_{dc}(s) + \frac{s}{U_{dc}\left(C_{dc}s^2 + K_{u1}K_1K_2s + T_{u1}K_1K_2\right)}P_d(s). \quad (32)$$

By analyzing the transfer function, it can be learned that the double closed-loop control involves certain inhibition ability to the perturbation power. However, the control of perturbation power needs to be indirectly adjusted through the voltage outer ring, which increases the adjusting time. Therefore, this paper will consider the output power of converter as the control inner ring. When the load power fluctuation is larger, it can directly act on the preset of converter power, which makes the power regulation avoid the control process of the voltage outer ring and effectively inhibits the bus voltage fluctuations brought by the load change.

*3.2. The Strategy of Power Inner Ring Control of Converter.* The capacitance energy of DC bus can be expressed as [31]

$$E_{dc} = \frac{1}{2}C_{dc}U^2_{dc}. \quad (33)$$

In the normal working process of the microgrid, through ignoring the power loss of the circuit devices themselves, and considering that the output power balance of the converter is equal to that of the power balance between photovoltaic and load, the capacitance energy of the DC bus remains unchanged, and the voltage of DC bus is stable [32]. The voltage of the DC bus is able to be controlled via commanding the stability of capacitance energy of the DC bus. Hence, this paper proposes a double closed-loop control strategy with the output power of converter as the control inner ring and the capacitance energy of the DC bus as the control outer ring, taking the supercapacitor as an example, shown in Figure 8. In Figure 8, $P_e$ is the compensation power (W) of the supercapacitor obtained after the power distribution and calculation of the perturbation power, and the output of the power inner ring is the instantaneous output power of the converter. In order to improve the mutational response performance of the system to the load power, the transfer function power of feedforward is introduced. And the changes of load power feedforward to the wave generating link of the converter, which constitutes a system with combining feedforward and feedback.

In Figure 8, $E_{dc}$ represents the capacitance energy of the DC bus; $P_{cap}$ is the instantaneous power of the bus capacitance (W); $P_{BDC}$ is on behalf of the output power of the bidirectional DC/DC converter; $G_P(s)$ acts as the transfer function of the PI controller of power inner ring; $G_{u2}(s)$ indicates the transfer function of the outer ring PI controller from the bus capacitance energy, of which the formula expression is

$$G_P(s) = K_P + \frac{T_P}{s}$$
$$G_{u2}(s) = K_{u2} + \frac{T_{u2}}{s}. \quad (34)$$

In the formula above, $K_p$ and $T_p$ are on behalf of the proportional coefficients and integral coefficients of the PI controller of power inner ring, respectively; $K_{u2}$ and $T_{u2}$ refer to the proportional coefficients and integral coefficients of the PI controller of outer ring, respectively.

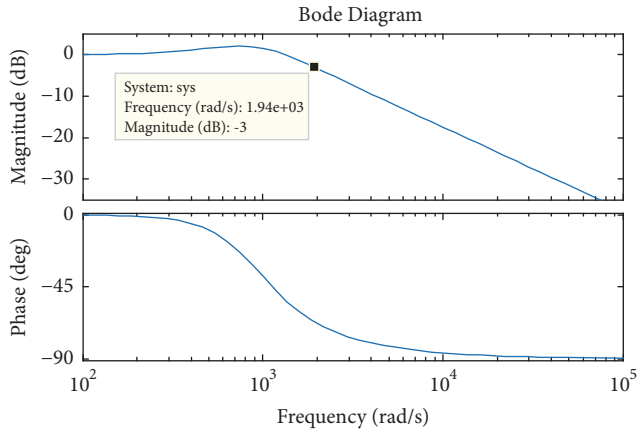


Figure 9: Frequency domain characteristic curve of power inner ring control of the system.

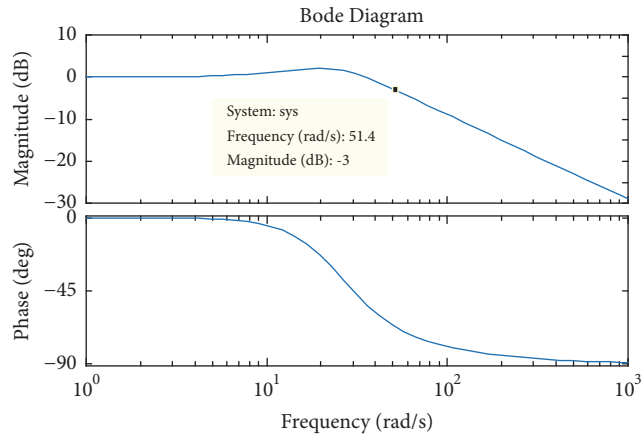


Figure 10: Characteristic curve of the frequency domain of bus capacitance energy control in the power inner ring.

According to Figure 8, the closed-loop transfer function of the controller of the power inner ring is

$$\frac{P_{\mathrm{BDC}}}{P^{*}_{\mathrm{BDC}}} = \frac{U_{\mathrm{sc}}K_p s + U_{\mathrm{sc}}T_p}{L_{\mathrm{sc}}s^2 + \left(U_{\mathrm{sc}}K_p + R_{\mathrm{sc}}\right)s + U_{\mathrm{sc}}T_p}. \tag{35}$$

The damping coefficient $\zeta_p$ and natural frequency $\omega_{np}$ of power inner ring are

$$\begin{aligned} \zeta_P &= \frac{U_{\mathrm{sc}}K_p R_{\mathrm{sc}}}{2\sqrt{L_{\mathrm{sc}}U_{\mathrm{sc}}T_p}}. \\ \omega_{np} &= \sqrt{\frac{U_{\mathrm{sc}}T_p}{L_{\mathrm{sc}}}} \end{aligned} \tag{36}$$

In order to strengthen the control effects, the bandwidth frequency of two loops requires thinking over, so as to avoid the interference between the inner ring and the outer ring. Setting the simulation parameters of system as $L_{\mathrm{sc}} = 0.003\mathrm{H}$, $R_{\mathrm{sc}} = 0.01\Omega$, and $U_{\mathrm{sc}} = 200\mathrm{V}$, according to the $\zeta_p = 0.707$PI parameter setting, the PI parameters of the power inner ring are calculated as

$$\begin{aligned} K_{p2} &= 0.02, \\ T_{p2} &= 13.4. \end{aligned} \tag{37}$$

The frequency domain characteristic curve of the power inner ring control of the system can be got as in Figure 9, and the bandwidth frequency of the system is $\omega_{bp} = 1.94 \times 10^3 rad/s$.

In terms of the double closed-loop control system, when the bandwidth of inner ring control is much larger than the outer ring and the gain of the inner ring in the control bandwidth is 0 ( the amplifying coefficient is 1), the amplifying coefficient of inner ring within the response spectrum in the systematic external ring is 1. So the power inner ring can be approximated to a proportional link that has a magnifying coefficient of 1, and the transfer function of outer loop is as follows:

$$E_{\mathrm{dc}} = \frac{K_{u2}s + T_{u2}}{s^2 + K_{u2}s + T_{u2}}E^{*}_{\mathrm{dc}} + \frac{\left(G_d(s) - 1\right)s}{s^2 + K_{u2}s + T_{u2}}P_{\mathrm{e}}. \tag{38}$$

The capacitance energy of DC bus in the formula is composed of two parts, which reflects the tracking characteristic of $E^{*}_{\mathrm{dc}}$ and the perturbation characteristic of $P_{\mathrm{e}}$ to the system, respectively. When satisfying $G_d(s) = 1$, the disturbance components contained in the system power can be completely eliminated. Therefore, the parameter setting of the control system can be carried out based on the coefficient of $E^{*}_{\mathrm{dc}}$. The damping coefficient $\zeta_{u2}$ and natural frequency $\omega_{n2}$ of the outer ring are demonstrated as

$$\begin{aligned} \zeta_{u2} &= \frac{K_{u2}}{2\sqrt{T_{u2}}} \\ \omega_{n2} &= \sqrt{T_{u2}}. \end{aligned} \tag{39}$$

According to the optimal damping ratio $\zeta_{u2} = 0.707$ of the adjusting PI parameters, it can be obtained that $K_{u2} = 35.35$, $T_{u2} = 625$, of which the frequency of domain characteristic curve of the system is shown in Figure 10, and at this time the bandwidth frequency of the capacitance energy outer ring is $\omega_{b2} = 51.4 rad/s$. Hence, when using the power inner ring control, the bandwidth of the control of the outer ring is much smaller than that of the inner ring, so as to avoid the mutual interference of the internal and external loop control.

## 4. Result and Discussion

To prove the effectiveness of the new double closed-loop control strategy, in this paper, a photovoltaic DC microgrid model under the impact load is constructed which makes simulations and experiments' comparison between the classical double closed-loop control strategy and the power inner ring control strategy, respectively.

Table 1: The main devices' parameters in the experiments.

| Devices | Numerical value |
|---|---|
| DC bus capacitance($\mu$F) | 1000 |
| Battery rated voltage (V) | 12 |
| Rated capacity(Ah) Battery | 38 |
| Super capacitance(F) | 7.5 |
| Rated power (W) of DC motor | 30 |
| Rated voltage(V) of DC motor | 24 |
| Rated current(A) of DC motor | 2.1 |

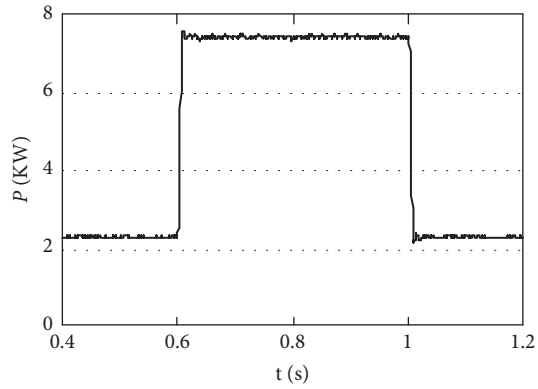


Figure 11: Power diagram of motor suddenly adding and reducing load.

*4.1. Simulation Result and Discussion.* On the basis of MATLAB/simulink, the simulation model shown in Figure 6 is established. And the motor speed is set as constant 2000r/min. With suddenly adding or reducing given value of the load of motor during normal operation, the suppression abilities of DC bus voltage of two control strategies are compared by simulation.

Figure 11 is used to show the motor load power waveform. The motor will reach the rated speed under the low load situation after power on, when the motor output power is 2.3KW. When on 0.6s, the sudden increased load to the motor can make the output power reach 7.4KW. While on 1s, unloading the motor load can render the motor restore low load operation state.

Figures 12 and 13 refer to the simulation waveforms adopting current inner ring and power inner ring, respectively. In terms of the two figures, $u_{dc}$ is used as the voltage (V) for DC bus; $i_{bat}$ is the current (A) of battery; $i_{sc}$ indicates the current (A)of super capacitor. As the distributed photovoltaic power source uses perturbation observation method to track the maximum power point, the DC bus voltage will be repeatedly shaken near the maximum power point.

Before 0.6s, the motor is in a low load operating state, the output power of the photovoltaic cell is bigger than the power consumption of motor, the energy storage system charges, and system steadily operates. On the 0.6s, the motor suddenly adds the load, the output power of the photovoltaic cell is less than the load power consumption, and energy storage system discharges. The DC bus voltage using the control strategy of the current inner loop has 14V of voltage drop, and the voltage drop of the DC bus is less than 3V when the control strategy of the power inner ring is employed. Besides, on the 1s, the motor suddenly reduces the load, the DC bus utilizing the current inner ring strategy has 15V of voltage surge, and the increment of the DC bus voltage that uses the power inner ring control strategy is less than 3V.

*4.2. Experiment Result and Discussion.* The controller of the experiments utilizes the DS1104 control board of the DSPACE control platform. And the energy storage device is composed of batteries and supercapacitors through the way that the photovoltaic cell simulator simulates the output characteristics of the photovoltaic cell. The schematic diagram and the physical diagram of the experimental device are shown in Figures 14(a) and 14(b). Of them, the main control board, acting as the core part of the experimental device, mainly includes the photovoltaic input interface and boost circuit, hybrid energy storage input interface and BDC circuit, and load output interface and buck circuit. Photovoltaic simulators, batteries, and supercapacitors are parallel to the DC bus through DC/DC converters, respectively. The DC motor serves as the impact load to test the control strategy of the performance of DC bus voltage stabilizer. The structural figure and the physical figure for the main control board are as shown in Figures 15(a) and 15(b). In addition, the main device parameters in the experiment are shown in Table 1.

Figure 16 presents the experimental waveform that adopts the power inner ring control strategy: $u_{dc}$ is the DC bus voltage (V), $i_{bat}$ indicates the battery current (A), and $i_{sc}$ is the

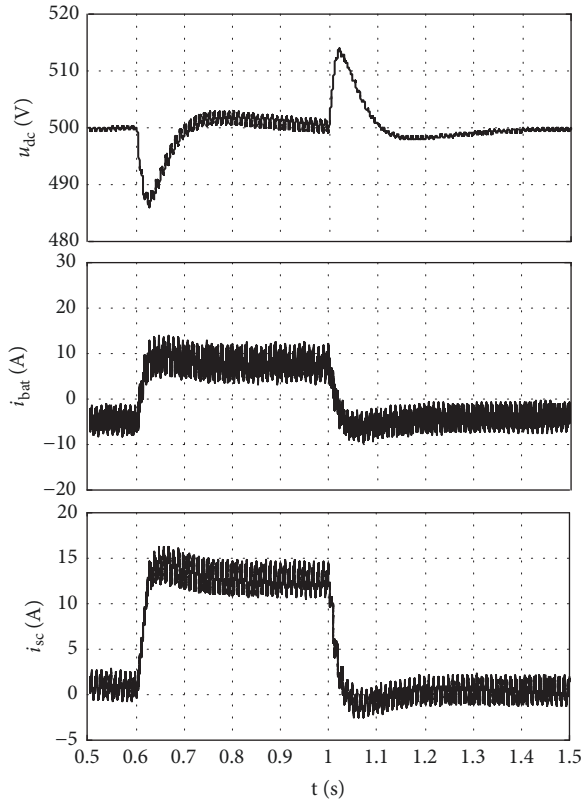


Figure 12: The control strategy of current inner ring.

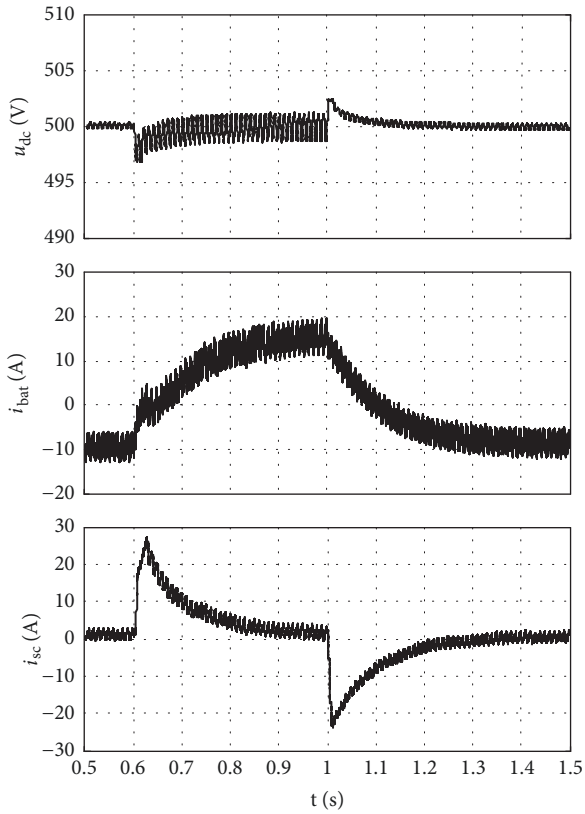


Figure 13: The control strategy of power inner ring.

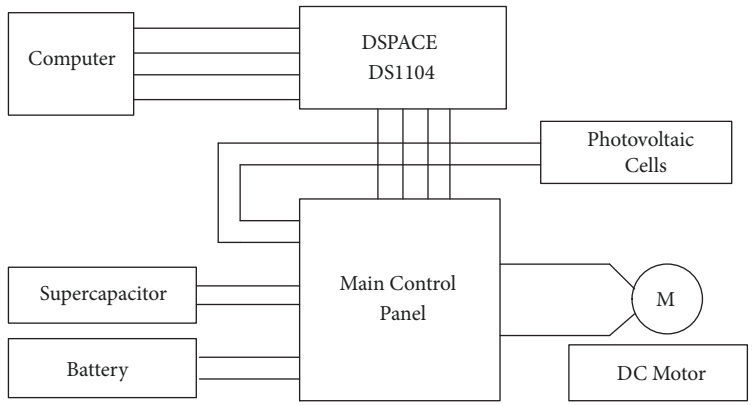


(a) Schematic diagram

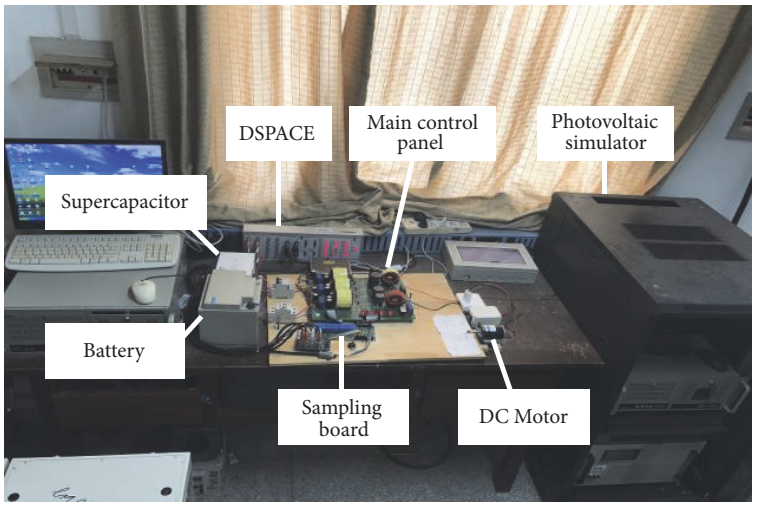


(b) Physical diagram

Figure 14: Experimental device diagram.

supercapacitance current (A). Under the initial conditions, the stable value of the DC bus voltage is set as 24V when the system power keeps balance, photovoltaic output is sufficient to maintain the bus voltage stability, and battery current $i_{bat}$ and current $i_{sc}$ of the supercapacitors are in the mixed energy storage output 0A.

As the load power on the DC bus increases when the DC motor is launched at 1.1s, the output power of the photovoltaic cell is less than the consumption power of the load, resulting in producing 1.9V voltage drop. At that moment, the batteries and the supercapacitors discharge to sustain the stability of the DC bus voltage. The battery maximally outputs current 3.8A and then gradually drops to 0.5A, while the supercapacitors maximally output current7.5A and gradually drop to 0.5A, and the DC bus voltage stabilizes rapidly in 24V.

On the 4.5s, the DC motor is turned off, the DC bus voltage produces 0.3V voltage rise, the output currents of batteries and supercapacitors are reduced to 0A, and the DC bus voltage is stable in the 24V.

Figure 17 is an experimental waveform of the start and stop of the motor when the current inner ring control strategy is adopted. When starting the motor at 1.1s, the DC bus produces 5.3V voltage drop, and the energy storage part compensates the system power. Therefore, the output current of the battery maximally reaches 6.3A, and the maximum output current of the supercapacitors reaches 7.2A. Because the energy storage part of the power compensation is too large, the DC bus voltage produces 1.1V voltage overshoots when it recovers, which results in the appearance of charging phenomenon of the supercapacitors, and manifests the bus voltage oscillation and gradual stability in 24V. When the DC motor is turned off at 4.3s, the DC bus voltage produces 0.3V voltage rise and quickly returns to stability, and the batteries and supercapacitors current drops to 0A.

Comparing the two experimental results, it can be observed that when the power fluctuation of the DC bus occurs, using the power inner ring control strategy is better conducive to allocate the compensating power of the battery and the supercapacitance, and giving full play to the advantage of the supercapacitors power density is beneficial to speedily compensate for the bus power. However, when adopting the inner loop control strategy of current, the energy storage part is sensitive to the current responses, which brings excessive compensation, overshooting the DC

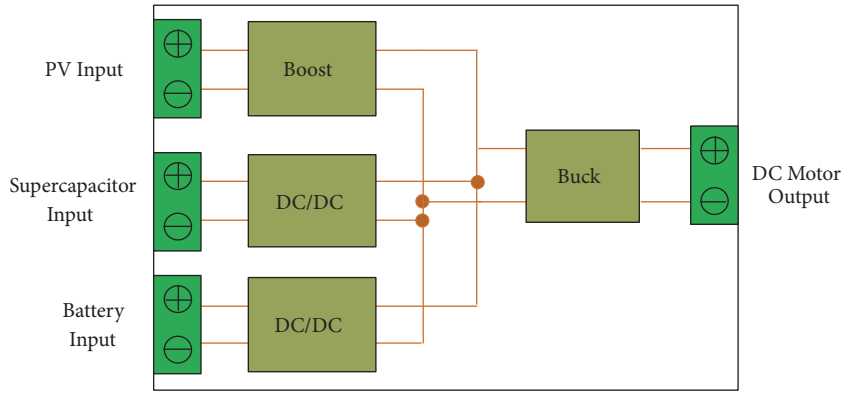


(a) Schematic diagram

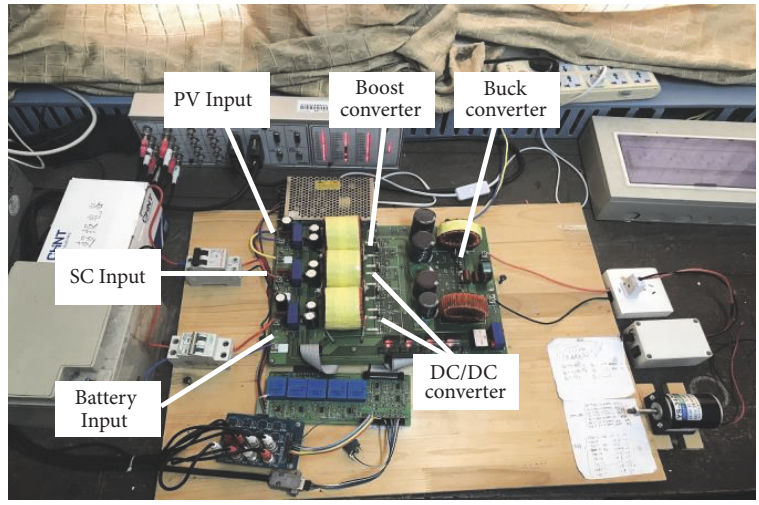


(b) Physical diagram

Figure 15: Main control panel.

bus voltage, and the charging phenomenon of supercapacitors as well as the reducing stability of the system.

The experiments in Figure 17 show that adopting the control strategies of power inner ring and the DC bus capacitors energy outer loop can effectively improve the voltage recovery competence of the DC bus when the load side produces larger power fluctuation.

## 5. Conclusion

In the past, the model of photovoltaic DC microgrid is rarely involved in the impact load, of which the voltage stability control of the DC bus is mainly concentrated on the research under conventional load power of the small fluctuation. In the light of this situation, this paper establishes a model of photovoltaic DC microgrid based on the impact load to study the problem of the steady voltage of DC bus under the impact load. It also optimizes the control strategy of energy storage converter and proposes a new double closed-loop control strategy for power inner ring and energy outer ring. Compared with the feedforward control and the observer control method, the power inner loop control does not need the extra real-time information of the acquisition system, lowers the system cost, improves its reliability, and does not introduce additional noises. The power inner ring control directly maps the changing trend of the output power to the wave-generating link, further improving the dynamic response characteristics of the converter. Besides, simulations and experiments verify the effectiveness of the power inner ring control strategy, and compared with the voltage-current double closed-loop control strategy and its improvement strategy, the impact of impulsive load on DC bus voltage fluctuation can be better suppressed.

## Data Availability

The data used to support the findings of this study are available from the corresponding author upon request.

## Conflicts of Interest

The authors declare that there are no conflicts of interest regarding the publication of this paper.

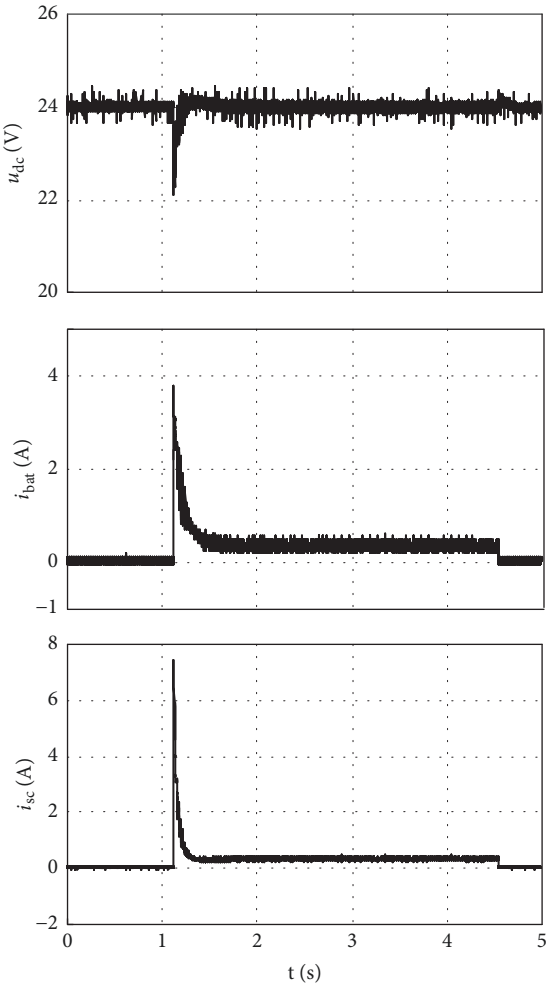


Figure 16: Experimental waveform using power inner ring control strategy.

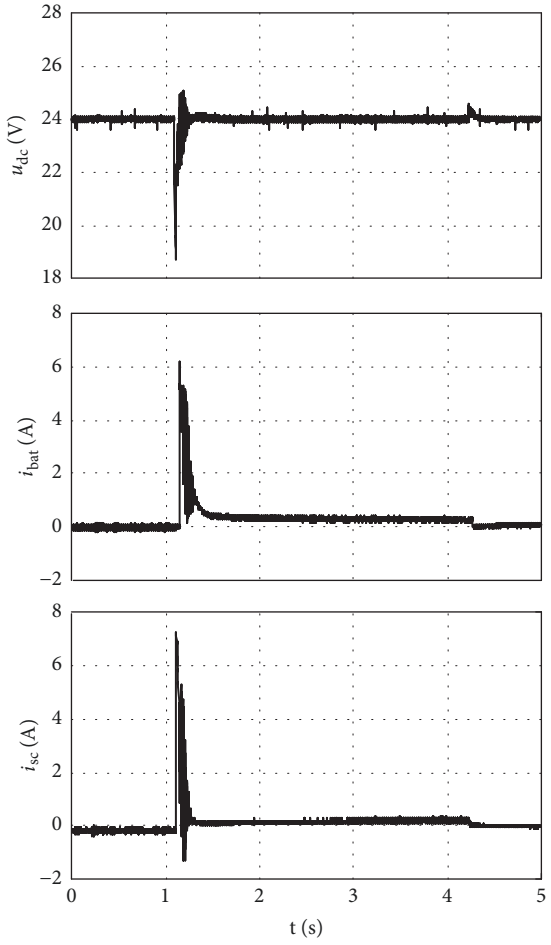


Figure 17: Experimental waveform using current inner ring control strategy.

## Acknowledgments

This work was supported by the Natural Science Foundation of China (no. 51567002) and the Guangxi Natural Science Foundation (no. 2017GXNSFAA198161).

## References

[1] E. O'Shaughnessy, D. Cutler, K. Ardani, and R. Margolis, "Solar plus: Optimization of distributed solar PV through battery storage and dispatchable load in residential buildings," *Applied Energy*, vol. 213, pp. 11–21, 2018.

[2] D. Wu, F. Tang, T. Dragicevic, J. C. Vasquez, and J. M. Guerrero, "A control architecture to coordinate renewable energy sources and energy storage systems in islanded microgrids," *IEEE Transactions on Smart Grid*, vol. 6, no. 3, pp. 1156–1166, 2015.

[3] F. A. Inthamoussou, J. Pegueroles-Queralt, and F. D. Bianchi, "Control of a supercapacitor energy storage system for microgrid applications," *IEEE Transactions on Energy Conversion*, vol. 28, no. 3, pp. 690–697, 2013.

[4] T. Vigneysh and N. Kumarappan, "Autonomous operation and control of photovoltaic/solid oxide fuel cell/battery energy storage based microgrid using fuzzy logic controller," *International Journal of Hydrogen Energy*, vol. 41, no. 3, pp. 1877–1891, 2016.

[5] A. P. Tahim, D. J. Pagano, E. Lenz, and V. Stramosk, "Modeling and stability analysis of islanded dc microgrids under droop control," *IEEE Transactions on Power Electronics*, vol. 30, no. 8, pp. 4597–4607, 2015.

[6] T. Pan, H. Liu, D. Wu, and Z. Hao, "Dual-layer optimal dispatching strategy for microgrid energy management systems considering demand response," *Mathematical Problems in Engineering*, vol. 2018, Article ID 2695025, 14 pages, 2018.

[7] Q. Lei, F. Z. Peng, and S. Yang, "Multiloop control method for high-performance microgrid inverter through load voltage and current decoupling with only output voltage feedback," *IEEE Transactions on Power Electronics*, vol. 26, no. 3, pp. 953–960, 2011.

[8] Y. C. Liang, X. U. Li-Chuan, and Y. G. Yan, "New start-up schemes for isolated boost converter in double close-loop control," *Proceedings of the Csee*, vol. 30, pp. 15–20, 2010.

[9] L. Tian, "Research on the voltage level selection and its stability control strategy of DC microgrid," *Power System Protection and Control*, vol. 45, no. 13, pp. 21–26, 2017.

[10] J. Sun, X. Dou, Z. Zhang, X. Quan, T. Xu, and P. Xu, "DC peer-to-peer coordinated control strategy of hybrid energy storage

system for microgrid," *Transactions of China Electrotechnical Society*, vol. 31, no. 4, pp. 194–202, 2016.

[11] S. Jin, Z. Mao, H. Li, and W. Qi, "Dynamic operation management of a renewable microgrid including battery energy storage," *Mathematical Problems in Engineering*, vol. 2018, Article ID 5852309, 19 pages, 2018.

[12] M. M. Abdelaziz and E. El-Saadany, "Maximum loadability consideration in droop-controlled islanded microgrids optimal power flow," *Electric Power Systems Research*, vol. 106, pp. 168–179, 2014.

[13] C. A. Hans, P. Braun, J. Raisch, L. Grune, and C. Reincke-Collon, "Hierarchical distributed model predictive control of interconnected microgrids," *IEEE Transactions on Sustainable Energy*, vol. 10, no. 1, pp. 407–416, 2019.

[14] C.-H. Liu and Y.-Y. Hsu, "Design of a self-tuning PI controller for a STATCOM using particle swarm optimization," *IEEE Transactions on Industrial Electronics*, vol. 57, no. 2, pp. 702–715, 2010.

[15] S. Quan, S. Hao, and L. Huang, "Novel double-closed-loop control for DC/DC converter with large voltage step-up ratio," *Electric Machines & Control*, vol. 15, no. 10, pp. 28–35, 2011.

[16] A. Khorsandi, M. Ashourloo, H. Mokhtari, and R. Iravani, "Automatic droop control for a low voltage DC microgrid," *IET Generation, Transmission & Distribution*, vol. 10, no. 1, pp. 41–47, 2016.

[17] V. Nasirian, A. Davoudi, F. L. Lewis, and J. M. Guerrero, "Distributed adaptive droop control for DC distribution systems," *IEEE Transactions on Energy Conversion*, vol. 29, no. 4, pp. 944–956, 2014.

[18] Y. Bao, L. Y. Wang, C. Wang, J. Jiang, C. Jiang, and C. Duan, "Adaptive feedforward compensation for voltage source disturbance rejection in DC–DC converters," *IEEE Transactions on Control Systems Technology*, vol. 26, no. 1, pp. 344–351, 2018.

[19] W. Jiang, Z. Wu, Y. Hu, and Y. She, "Dc capacitance energy storage feedback and load power feedforward boost converter control strategy," *Electric Power Automation Equipment*, vol. 34, no. 08, pp. 103–107, 2014.

[20] S. Wi and M. Kim, "Precise control strategy of dual-mode flyback DC/DC converter," *IET Power Electronics*, vol. 12, no. 2, pp. 220–227, 2019.

[21] L. Yi-Hung, "A novel reduced switching loss bidirectional AC/DC converter PWM strategy with feedforward control for grid-tied microgrid systems," *IEEE Transactions on Power Electronics*, vol. 29, no. 3, pp. 1500–1513, 2014.

[22] G. Mademlis, G. K. Steinke, and A. Rufer, "Feed-forward-based control in a DC–DC converter of asymmetric multistage-stacked boost architecture," *IEEE Transactions on Power Electronics*, vol. 32, no. 2, pp. 1507–1517, 2017.

[23] S. Kouro, P. Lezana, M. Angulo, and J. Rodriguez, "Multicarrier PWM with DC-link ripple feedforward compensation for multilevel inverters," *IEEE Transactions on Power Electronics*, vol. 23, no. 1, pp. 52–59, 2008.

[24] D. Dong, I. Cvetkovic, D. Boroyevich, W. Zhang, R. Wang, and P. Mattavelli, "Grid-interface bidirectional converter for residential DC distribution systems—part one: high-density two-stage topology," *IEEE Transactions on Power Electronics*, vol. 28, no. 4, pp. 1655–1666, 2013.

[25] L. Guo, X. Li, and C. Wang, "Coordinated control of hybrid power supply systems considering non-linear factors," *Proceedings of the CSEE*, vol. 32, pp. 60–69, 2012.

[26] A. Sato and T. Noguchi, "Voltage-source PWM rectifier–inverter based on direct power control and its operation characteristics," *IEEE Transactions on Power Electronics*, vol. 26, no. 5, pp. 1559–1567, 2011.

[27] O. Ibrahim, N. Z. Yahaya, N. Saad, and K. Y. Ahmed, "Development of observer state output feedback for phase-shifted full bridge DC–DC converter control," *IEEE Access*, vol. 5, pp. 18143–18154, 2017.

[28] C. Wang, X. Li, L. Guo, and Y. W. Li, "A nonlinear-disturbance-observer-based DC-Bus voltage control for a hybrid AC/DC microgrid," *IEEE Transactions on Power Electronics*, vol. 29, no. 11, pp. 6162–6177, 2014.

[29] H. Tsai, "Insolation-oriented model of photovoltaic module using Matlab/Simulink," *Solar Energy*, vol. 84, no. 7, pp. 1318–1326, 2010.

[30] W. Li, G. Joos, and J. Belanger, "Real-time simulation of a wind turbine generator coupled with a battery supercapacitor energy storage system," *IEEE Transactions on Industrial Electronics*, vol. 57, no. 4, pp. 1137–1145, 2010.

[31] L. Michels, S. V. Oliveira, A. Péres, and R. D. Reiter, "Digital resonant controller for dual-stage photovoltaic inverter system with small dc-bus capacitor," *IET Power Electronics*, vol. 9, no. 6, pp. 1315–1321, 2016.

[32] M. Karimi-Ghartemani, S. A. Khajehoddin, P. Jain, and A. Bakhshai, "A systematic approach to dc-bus control design in single-phase grid-connected renewable converters," *IEEE Transactions on Power Electronics*, vol. 28, no. 7, pp. 3158–3166, 2013.